The Astrophysical Journal, 705:1594–1606, 2009 November 10 doi:10.1088/0004-637X/705/2/1594

DECELERATING RELATIVISTIC TWO-COMPONENT JETS

Z. Meliani[1] and R. Keppens[1,2,3]
[1] Centre for Plasma Astrophysics, K.U.Leuven, Belgium; Zakaria.Meliani@wis.kuleuven.be, Rony.Keppens@wis.kuleuven.be
[2] FOM-Institute for Plasma Physics Rijnhuizen, Nieuwegein, Netherlands
[3] Astronomical Institute, Utrecht University, Netherlands
Received 2009 June 25; accepted 2009 October 5; published 2009 October 23

ABSTRACT

Transverse stratification is a common intrinsic feature of astrophysical jets. There is growing evidence that jets in radio galaxies consist of a fast low-density outflow at the jet axis, surrounded by a slower, denser, extended jet. The inner and outer jet components then have a different origin and launching mechanism, making their effective inertia, magnetization, associated energy flux, and angular momentum content different as well. Their interface will develop differential rotation, where disruptions may occur. Here we investigate the stability of rotating, two-component relativistic outflows typical for jets in radio galaxies. For this purpose, we parametrically explore the long-term evolution of a transverse cross section of radially stratified jets numerically, extending our previous study where a single, purely hydrodynamic evolution was considered. We include cases with poloidally magnetized jet components, covering hydro and magnetohydrodynamic (MHD) models. With grid-adaptive relativistic MHD simulations, augmented with approximate linear stability analysis, we revisit the interaction between the two jet components. We study the influence of dynamically important poloidal magnetic fields, with varying contributions of the inner component jet to the total kinetic energy flux of the jet, on their non-linear azimuthal stability. We demonstrate that two-component jets with high kinetic energy flux and inner jet effective inertia which is higher than the outer jet effective inertia are subject to the development of a relativistically enhanced, rotation-induced Rayleigh–Taylor-type instability. This instability plays a major role in decelerating the inner jet and the overall jet decollimation. This novel deceleration scenario can partly explain the radio source dichotomy, relating it directly to the efficiency of the central engine in launching the inner jet component. The FRII/FRI transition could then occur when the relative kinetic energy flux of the inner to the outer jet grows beyond a certain threshold.

Key words: galaxies: jets – ISM: jets and outflows – methods: numerical – relativity

Online-only material: color figures

1. INTRODUCTION

There is strong observational and theoretical evidence that magnetic fields play a crucial role in the acceleration and the collimation of extragalactic jets. Most active galactic nuclei (AGNs) jet formation scenarios involve magnetic fields, threading a rotating black hole (in the ergosphere) and its accretion disk, thereby removing from them angular momentum, allowing the central black hole to accrete. At least close to the jet launching region, the jet rotation profile persists, reflecting its (general relativistic and/or magnetorotational) origin. Thus both ingredients, magnetic fields and rotation, are very important in jet formation, as well as in jet propagation and stability.

Moreover, detailed astrophysical jet observations point out that relativistic jets are structured, in a direction perpendicular to the jet axis, typically consisting of a fast spine and slower outer flow. In the case of AGNs, this jet structuring plays an important role in explaining the morphology of the jet high energy radiation (Ghisellini et al. 2005; Hardcastle 2006; Jester et al. 2006, 2007; Siemiginowska et al. 2007; Kataoka et al. 2008), with sometimes clear evidence for a very fast, light inner jet and a heavy slow outer outflow (Giroletti et al. 2004). Furthermore, observations of the TeV BL Lacertae objects show brightenings and rapid variability in their TeV emission. This variation in their high-energy emission implies high Lorentz factor flows occurring at smaller scale, suggesting ultra-relativistic bulk motion of the (inner) jet. At the same time, complementary (radio) observations with very long baseline interferometry of the pc-scale jet structure indicate a broad, "slowly" (albeit relativistic) moving outflow. In combination, this clearly suggests the presence of a two-component jet morphology (Ghisellini et al. 2005). A two-component jet structure has also been proposed in more theoretical work, addressing the physics of jet launching, collimation, and propagation mechanisms (Bogovalov & Tsinganos 2001; Sol et al. 1989; Meier 2003).

While our jet dynamics computations will be representative for AGN jet conditions, radially structured jet flows are now known to exist in virtually all astrophysical jet outflows. Transversely structured, ultra-relativistic jet-like outflow has been proposed in the context of gamma-ray bursts (Racusin et al. 2008) to explain the break observed in their afterglow light curve. In the case of stellar outflows, recent observations of some T Tauri jets (Bacciotti et al. 2000; Günther et al. 2009) also suggest a fast inner outflow bounded by a slow outer outflow. In these young stellar objects, a clear signature of jet rotation around the symmetry axis was detected (Bacciotti et al. 2002; Woitas et al. 2005; Coffey et al. 2004, 2007), fully supporting scenarios of magnetocentrifugal jet launch and acceleration. Theoretical models of two-component jets in classical T Tauri (Bogovalov & Tsinganos 2001; Meliani et al. 2006a; Cranmer 2008; Fendt 2009) then postulate that the inner outflow is turbulent and pressure driven, associated with the young star wind. The inner jet then has a small opening angle, as it is collimated by the outer jet, which is in turn magnetocentrifugally driven from the surrounding disk. The outer disk wind then carries most of the mass loss in the jet. Various authors (Meliani et al. 2006a; Fendt 2009) have demonstrated using axisymmetric magnetohydrodynamic (MHD) simulations that

the outer outflow is self-collimated by its intrinsic magnetic field, and that the turbulent inner outflow gets collimated by the outer jet. Furthermore, Matsakos et al. (2008) investigated the topological stability of two-component outflows for young stellar objects, performing extensive numerical simulations to determine whether analytic self-similar models demonstrate robustness in axisymmetric conditions.

Also for relativistic jet simulations, axisymmetric assumptions are often adopted, excluding the development of all non-axisymmetric perturbations. These can address details of how helical field configurations (naturally expected from magneto-centrifugal launch mechanisms) effectively may transport their helicity down the jet beam (Keppens et al. 2008), with magnetically aided re-acceleration by field compression across internal cross shocks. While Keppens et al. (2008) concentrated on kinetic energy dominated jets, initially Poynting flux dominated jets were simulated by Komissarov et al. (2007) in axisymmetric relativistic MHD, finding that the transition to a matter-dominated jet regime occurs very close to the central engine (within 0.01 pc). Our model computations will therefore assume kinetic-energy-dominated jets.

As far as the magnetic field topology is concerned, we will restrict ourselves in this paper to purely poloidally magnetized jet components. Our two-component jet model determining our initial conditions can actually allow for helical fields, as explained in Section 2 (we include this more general case here for future reference in follow-up studies). As indicated before, during the first acceleration phase of AGN jets, magneto-centrifugal mechanisms play an important role, and a helical or even strongly toroidal magnetic field is likely produced (Fendt 1997; Meliani et al. 2006b; McKinney & Blandford 2009; Komissarov et al. 2007). McKinney & Blandford (2009) present three-dimensional (3D) general relativistic MHD simulations for rapidly rotating black holes, producing jets with strong toroidal fields. They find a prominent role of the accreted magnetic field geometry for achieving "stable" jets. Helical or strongly toroidal field topologies can be subject to current-driven kink instabilities (Begelman 1998), with $m = 1$ toroidal modes that helically displace the jet axis. This requires full 3D numerical simulations, such as performed by Baty & Keppens (2002) in non-relativistic MHD, or addressed by Mizuno et al. (2009) in relativistic MHD for a static force-free equilibrium. Dispersion relations for non-axisymmetric modes and $m = 1$ kinks in particular for relativistic MHD were analyzed by Begelman (1998) for purely toroidal fields, and electromagnetically dominated force-free jets were analyzed spectrally by Istomin & Pariev (1996) and more recently by Narayan et al. (2009).

In our work, we will restrict attention to 2.5-dimensional (2.5D) scenarios with the somewhat unusual assumption of translational invariance along the jet axis. The overall configuration is schematically indicated in Figure 1, and we simulate a transverse cross section of the jet at a sufficient distance from the two-component jet source, where all the three velocity components (axial, azimuthal, and radial) are included, but their variation along the jet axis is ignored. Our aim is to investigate all non-axisymmetric instabilities, primarily induced by the (sheared) rotation. This approximation is valid because in the poloidal direction, the flow is supersonic with a high Lorentz factor, and then the growth rate of poloidal instabilities is expected to be low. On the other hand, the rotation is subsonic, facilitating the growth of toroidal instabilities. We then address jet stability in a cross section of a rotating two-component jet, initially collimated by thermal pressure and/or a poloidal magnetic field. Consecutive snapshots of the cross-sectional evolution can be interpreted as mimicking the jet flow conditions at an increasing distance from the source. Note that this particular assumption allows us to follow both axisymmetric and all non-axisymmetric (including $m = 1$) mode development, but does exclude helical mode axis displacement typical for kink modes. Our model therefore mimics jet evolution adequately as long as the radial axis displacement is smaller than the axial wavelength associated with possible $m = 1$ kinks. Our assumption does also neglect conical jet expansion, assuming cylindrical propagation. This is justified given the low observed values for jet opening angles.

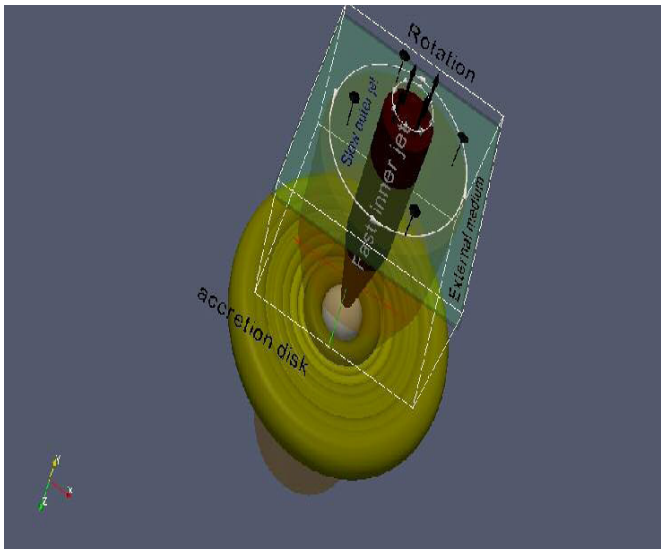

Figure 1. Three-dimensional schematic view of the overall AGN disk-jet configuration (indicating the accretion disk and the two-component jet). We model the jet evolution in the transverse plane.

(A color version of this figure is available in the online journal.)

Since we defer the study of toroidal and helical magnetic field configurations in 2.5D and 3D to later work, we start off with numerically investigating the influence of a purely poloidal magnetic field on the stability of rotating, two-component relativistic jets. Our work complements the studies looking into kink development by putting the emphasis on the azimuthal variation and on the effect of the two-component jet stratification. As far as a purely poloidal magnetic field topology is concerned, the work by Spruit et al. (1997) suggests that jets should be collimated by poloidal magnetic field pressure, rather than by toroidal magnetic field, as toroidal jet magnetic fields can introduce kink instability (but only slow mode growth was found for force-free jets by Narayan et al. 2009). To justify purely toroidal fields, we can argue that the toroidal magnetic field in the jet acceleration phase can be gradually dissipated involving reconnection, a mechanism which in turn contributes to (axial) jet acceleration (Spruit 2009; Meliani et al. 2006a). Indeed, during the acceleration phase a fraction of the Poynting flux (angular momentum) carried by the the magnetic field is converted to kinetic energy by internal dissipation/reconnection of the toroidal magnetic field (Spruit 2009; Meliani et al. 2006a). In accord with this mechanism, we model the region where the eventual jet rotation is low.

In this paper, we analyze five cases in detail to determine the effects of differing poloidal magnetic field configurations in the two-component structure on its long-term stability, and on the overall deceleration of the jet as it propagates away from

the central source regions. The role of the poloidal magnetic field is in these cases most prominent in its added effect on total pressure and effective fluid inertia, and this is shown to play a prominent role in the two-component jet stability.

2. TWO-COMPONENT JET MODEL

We set up a relativistic magnetohydrodynamic model of a two-component jet, which elaborates on the earlier model described in Meliani & Keppens (2007). The jet model uses as its basic characterizing parameter a total jet kinetic luminosity flux typical for powerful radio loud galaxies, namely $L_{\rm jet,Kin} = 10^{46}$ erg s^{-1} (Rawlings & Saunders 1991; Tavecchio et al. 2004). Second, the outer radius of the two-component jet is taken to be $R_{\rm out} \sim 0.1$ pc. This is a value directly inferred from observed values for M87 (Biretta et al. 2002), which has a known jet opening angle of 6° at 1 pc from the jet source. For the less constrained inner jet radius, we adopt the initial value $R_{\rm in} = R_{\rm out}/3$. The remainder of the $t = 0$ condition is then characterized by the velocity profiles in both inner and outer jet components and by the magnetic configuration in the two-component jet.

2.1. Initial Flow Profiles and Rayleigh Criterion

For the initial flow condition, we adopt a uniform outflow velocity V_z along the jet axis in each jet component, with $V_{\rm z,out} = 0.9428$ (hence $\gamma_{\rm z,out} \sim 3$, since speeds are normalized to the light speed) for the outer, slow jet located within $R_{\rm in} < R < R_{\rm out}$. This represents a typical outflow value for relativistic jets at a parsec scale from the source. The inner jet has a much faster outflow speed, which we set to $V_{\rm z,in} = 0.99939$, with the corresponding Lorentz factor $\gamma_{\rm z,in} \sim 30$. The difference in the Lorentz factor by an order of magnitude in the inner versus outer jet layers is representative (though somewhat exaggerated) for differences inferred for the BL Lac object Markarian 501 between its central spine and surrounding (shear) layer jet, as described by Giroletti et al. (2004). However, it remains lower than the Lorentz factor $\gamma \sim 50$ suggested for TeV blazar PKS 2155−304 (Ghisellini & Tavecchio 2008).

Two-component jet models also commonly assume that the spin of the inner beam is higher than the spin of the outer jet. The physical argument is that the inner beam is extracting angular momentum from the inner parts of the accretion disk and from the black hole itself, both implying fast rotation. Therefore, we adopt different initial rotation profiles for the inner versus outer jet, both radially self-similar. Although in our numerical results below we will only adopt purely poloidal magnetic field configurations, i.e., we will have $\vec{B} = B_z(R, \varphi; t)\vec{e}_z$, one can generalize our initial equilibrium configuration to allow for both toroidal speeds and toroidal magnetic fields, sharing the same R dependence. In that general case, one takes in practice

$$V_\varphi = \begin{cases} v_{\varphi,\rm in}\left(\dfrac{R}{R_{\rm in}}\right)^{a_{\rm in}/2} & R \leqslant R_{\rm in}, \\ v_{\varphi,\rm out}\left(\dfrac{R}{R_{\rm in}}\right)^{a_{\rm out}/2} & R_{\rm in} < R < R_{\rm out}\,, \end{cases} \quad (1)$$

$$B_\varphi = \begin{cases} b_{\varphi,\rm in}\left(\dfrac{R}{R_{\rm in}}\right)^{a_{\rm in}/2} & R \leqslant R_{\rm in}, \\ b_{\varphi,\rm out}\left(\dfrac{R}{R_{\rm in}}\right)^{a_{\rm out}/2} & R_{\rm in} < R < R_{\rm out}, \end{cases} \quad (2)$$

where the $\vec{V} = V_\varphi\vec{e}_\varphi + V_z\vec{e}_z$ is the 3-velocity, and similarly for the magnetic field. At $t = 0$, we then have a discontinuity in the toroidal velocity at the boundary between the two jets when fixing $v_{\varphi,\rm in} = 0.01$ and $v_{\varphi,\rm out} = 0.001$. A faster rotating inner component is consistent with a small expansion of the inner streamlines, which are confined by the outer outflow. The fast rotating inner jet effectively extracts the angular momentum from the central region and carries it away with a very small mass flux. In fact, our models typically have the inner jet extracting order 10% of the total angular momentum associated with the two-component jet. We fix the exponent $a_{\rm in} = 0.5$ for the inner jet and $a_{\rm out} = -2$ for the outer jet. We then choose for the outer jet a rotation profile implying a radially constant angular momentum. This is motivated by the fact that this component is believed to be launched from an accretion disk, where the outer streamlines in the jet expand faster than the inner streamlines.

The rotation profile of the inner jet then obeys the relativistic equivalent of the Rayleigh criterion for stability, namely that the angular momentum flux given by

$$I = \gamma\frac{\left(\rho + \frac{\Gamma}{\Gamma-1}p\right)}{\rho}V_\varphi R - \frac{B_{\rm p}}{\gamma\,\rho\,V_{\rm p}}R\,B_\varphi \quad (3)$$

increases with R (Meliani et al. 2006b). This expression uses proper density and pressure ρ, p, assumes a polytropic index Γ appearing in a simple polytropic equation of state (our actual numerical simulations will in fact relax this assumption and use a full Synge-type equation of state), and writes V_p, B_p for poloidal 3-velocity and magnetic field strengths. For the chosen radial prescriptions for V_φ given by Equation (1), we have for the inner jet

$$\frac{d|I|}{dR} \propto (a_{\rm in}/2 + 1) > 0, \quad (4)$$

making the inner jet centrifugally stable. The outer outflow, on the other hand, is marginally stable, following the same argument. In the numerical simulations further in this paper, we neglect the toroidal field B_φ, and then the interface between the two components does not verify the Rayleigh criterion, and this shear flow interface is unstable from the start, since the angular momentum at the interface decreases when

$$\gamma_{\rm out}\frac{\left(\rho_{\rm out} + \frac{\Gamma_{\rm out}}{\Gamma_{\rm out}-1}p_{\rm out}\right)}{\rho_{\rm out}}v_{\varphi,\rm out} < \gamma_{\rm in}\frac{\left(\rho_{\rm in} + \frac{\Gamma_{\rm in}}{\Gamma_{\rm in}-1}p_{\rm in}\right)}{\rho_{\rm in}}v_{\varphi,\rm in}. \quad (5)$$

This means that in all cases we will simulate the initial shear flow interface at $R = R_{\rm in}$, develop small-scale instabilities, and intend to address the ultimate nonlinear stability of such initial two-component structure. The central question investigated then is whether the dynamics will lead to complete destruction of the initial two-component nature of the outflow at further distances from the source. Related to this question, we will quantify the potential deceleration of the central fast jet by mixing processes, induced by the nonlinear evolution of the two-component jet.

2.2. Initial Densities and Magnetic Configuration

The densities and poloidal magnetic field B_z are assumed to be constant within the three different regions, namely throughout inner jet beam, outer jet, and external region. The external medium is hot and rarified and has a small reference number density. The typical ISM number density value of 1 cm^{-3} is in the computation used as a scaling value. We arbitrarily set $\rho_{\rm med} = m_p n_{\rm med}$ with $n_{\rm med} = 10^{-2}$ cm^{-3}, and adopt $c = 1$

and a unit of length of 1 pc. This sets the unit of pressure, and a corresponding scaling value for the magnetic field is then 0.1375 Gauss (as mass is normalized to proton mass m_p).

The jet environment represents a relativistically hot, rarified, static external medium. This is consistent with the fact that at the parsec scale, the jet head has previously shocked the jet surroundings, so that the jet itself gets embedded in a dilute, hot medium. Assuming a number density for this external medium of $n_{\rm med} = 10^{-2}$ cm^{-3} is appropriate, since this is near values obtained in numerical simulations of jet propagation and is then typical for the jet cocoon surroundings (Meliani et al. 2008). Values for the jet component proper densities are estimated from the kinetic luminosity flux and its division over inner and outer jet components. Requiring that the outer jet carries a case-specific fraction of the total kinetic luminosity flux by

$$f_{\rm out} L_{\rm jet,Kin} = (\gamma_{\rm out}\, h_{\rm out} - 1)\rho_{\rm out}\gamma_{\rm out}\pi\left(R_{\rm out}^2 - R_{\rm in}^2\right)V_{\rm out}, \quad (6)$$

we can deduce the density $\rho_{\rm out}$, if we, in addition, prescribe the (outer) jet Lorentz factor and make the initial approximation that the thermal energy in the outer jet is negligible compared to its mass energy (as valid in all cases studied). In Equation (6), $h_{\rm out}$ is the specific enthalpy in the outer jet, and its expression depends on the equation of state. When we consider that the inner component carries only a small fraction $f_{\rm in} = 1\%$ of the total kinetic luminosity flux, such that the outer jet carries the remaining $f_{\rm out} = 99\%$, we find that the resulting density is $\rho_{\rm out} \sim 119.94 \times 10^2 \rho_{\rm med}$. A similar argument for the inner, light jet, works out to fix $\rho_{\rm in} \sim 6.92\rho_{\rm med}$.

While in all cases, we investigate here numerically, we assume these initial, piecewise constant, densities for the inner and outer jets, the actual kinetic luminosity carried by each component will change from one case to another. This relates to our prescription of the pressure and magnetic variation in the jet components, and we will simulate five cases with varying thermal pressure contribution at the jet axis. In four cases (A), (B2), (C), and (D), the total pressure at the jet axis ends up similarly, while case (B1) has a lower total pressure value. By varying the relative contribution of thermal to magnetic pressure in the jet components, we aim to analyze the effect on overall jet stability of varying magnetic field and kinetic energy contributions to the kinetic luminosity in each component. In all five cases studied, we set the pressure of the external medium to ensure total pressure balance with the outer jet. Also, in the four cases (A), (B1), (C), and (D), we assume that the thermal energy in the inner (hot) component is higher than its mass energy. Only in case (B2), the thermal energy is lower than the mass energy. They differ in the following sense: in the first case (A), both components are non-magnetized, and the pressure at the jet axis is $p_0 = 2.3$ in our simulation units. This purely hydrodynamic case differs from the hydro case already studied in Meliani & Keppens (2007), as now the inner jet has an even higher Lorentz factor, a slightly different inner rotation profile, and an on-axis pressure value which makes the entire inner jet relativistically hot. In cases (B1) and (B2), only the inner jet is magnetized, and we set it to a constant value $B_{\rm z,in} = \sqrt{0.01\gamma_{\rm in}^2\rho_{\rm in}} \sim 0.789$ (making the jet parameter $\sigma = B_z^2/(\gamma^2\rho)$ expressing magnetic to rest-mass energy of order 0.01, as for kinetic energy dominated jets) in case (B1) and $B_{\rm z,in} \sim 2.28$ in case (B2). In case (B1), the thermal pressure on axis is set to $p_0 = 0.1$, and in case (B2) the thermal pressure on axis is $p_0 = 10^{-4}$. In case (C), only the outer jet is magnetized with $B_{\rm z,out} = \sqrt{0.005\gamma_{\rm out}^2\rho_{\rm out}} \sim 2.323$, and we adopt the same order on-axis inner pressure as in (A), namely $p_0 \approx 2.3$. In case (D), both inner and outer jets are magnetized, with $B_{\rm z,in} \sim 0.789$ and $B_{\rm z,out} \sim 2.323$. We then take the pressure at the jet axis $p_0 \approx 2$. In all magnetized cases, the magnetic field strength is set according to the observations at parsec scale (O'Sullivan & Gabuzda 2009). Clearly, in all four cases (A), (B1), (C), and (D), the thermal energy in the inner component dominates, only in case (B2) the thermal energy is lower than the mass energy. The pressure profile through inner and outer jets is taken from transverse equilibrium conditions, discussed next.

2.3. Two-component Jet Pressure Profiles

Since we assume an initial near steady-state axisymmetric two-component jet, the actual pressure variation is deduced from transverse equilibrium among pressure gradient, centrifugal force, and Lorentz force. This is expressed by the steady-state equation (Meliani et al. 2006b; Appl & Camenzind 1993; Heyvaerts & Norman 2003)

$$\gamma\rho\vec{V}\cdot\nabla(\gamma h\vec{V}) = -\nabla p + \rho_e\vec{E} + \vec{J}_{\rm e}\wedge\vec{B}. \quad (7)$$

Here ρ is the proper density of particles, p and h are the pressure and enthalpy per particle, respectively, $\vec{V}$ is the fluid 3-velocity, γ is the Lorentz factor, and $(\vec{E},\vec{B})$ denote the electromagnetic fields. We have $\rho_{\rm e} = \nabla\cdot\vec{E}$ and for steady-state conditions $\vec{J}_{\rm e} = \nabla\wedge\vec{B}$ as the associated charge and current densities, while $\vec{E} = -\vec{V}\wedge\vec{B}$ in ideal relativistic MHD.

If we introduce the total pressure in the fluid frame,

$$\psi = p + \frac{B^2 - E^2}{2} = p + \frac{B_z^2 + B_\varphi^2}{2} - \frac{(B_\varphi V_z - V_\varphi B_z)^2}{2}, \quad (8)$$

the radial component of Equation (7) can be written as

$$\frac{d\psi}{dR} - \frac{\Gamma}{\Gamma-1}\frac{\gamma^2 V_\varphi^2}{R}\psi = \frac{\gamma^2 V_\varphi^2}{R}\left(\rho - \frac{\Gamma}{\Gamma-1}\frac{B_z^2}{2}\right) + \frac{1}{R}\left(1 + \frac{\Gamma\gamma^2 V_\varphi^2}{2(\Gamma-1)}\right)\left(-B_\varphi^2 + \left(B_\varphi V_z - V_\varphi B_z\right)^2\right). \quad (9)$$

This has assumed a polytropic equation of state. We can then determine the radial pressure profile $p(R)$ by solving the first-order differential Equation (9) and using Equation (8), together with the self-similar prescriptions from Equations (1) and (2) to get

$$p = \zeta\left(1 - \alpha\left(\frac{R}{R_{\rm in}}\right)^a\right)^{-\frac{\Gamma}{a(\Gamma-1)}} - \frac{(\Gamma-1)}{\Gamma}\rho - \frac{(\Gamma-1)(a+2)}{2\alpha(a(\Gamma-1)+\Gamma)}\left(-b_\varphi^2 + \left(b_\varphi V_z - v_\varphi B_z\right)^2\right) \times\left(1 - \alpha\left(\frac{R}{R_{\rm in}}\right)^a\right). \quad (10)$$

In this expression, the constant a is a self-similarity exponent, which we use to set the inner jet exponents $a_{\rm in}$ and the outer $a_{\rm out}$, and the constant $\alpha = \frac{v_\varphi^2}{1-V_z^2}$, which is different for inner versus outer jet $\alpha_{\rm in}, \alpha_{\rm out}$. Also, ζ is an integration constant, which is to be deduced from boundary conditions. For the inner jet, we use

it to set the pressure on axis p_0 from

$$\zeta_{\rm in} = p_0 + \frac{(\Gamma_{\rm in}-1)}{\Gamma_{\rm in}}\rho_{\rm in} + \frac{(\Gamma-1)\,(a+2)}{2\,\alpha\,(a\,(\Gamma-1)+\Gamma)}\left(-b_\varphi^2+\left(b_\varphi V_z - v_\varphi B_z\right)^2\right). \quad (11)$$

To fix the constants for the outer jet, we have to match conditions at the interface between the two components. At the contact between the two components, Rankine–Hugoniot conditions should hold. In terms of effective total pressure (Equation (8)) obeying Equation (9), we need to match at the interface

$$\psi_{\rm in}(R_{\rm in}) = \psi_{\rm out}(R_{\rm in}). \quad (12)$$

This yields for the constant pressure integration in Equation (10) for the outer jet

$$\zeta_{\rm out} = \left[\psi_{\rm in}(R_{\rm in}) + \frac{\Gamma_{\rm out}-1}{\Gamma_{\rm out}}\rho_{\rm out} - \frac{B_{z,\rm out}^2}{2}\right](1-\alpha_{\rm out})^{\frac{\Gamma_{\rm out}}{a_{\rm out}(\Gamma_{\rm out}-1)}} + \left[-b_{\varphi,\rm out}^2 + (b_{\varphi,\rm out}V_{z,\rm out} - v_{\varphi,\rm out}B_{z,\rm out})^2\right] \times (1-\alpha_{\rm out})^{\frac{\Gamma_{\rm out}}{a_{\rm out}(\Gamma_{\rm out}-1)}} \times \left(\frac{1}{2} + \frac{(1-\alpha_{\rm out})(\Gamma_{\rm out}-1)(a_{\rm out}+2)}{2\,\alpha_{\rm out}[a_{\rm out}(\Gamma_{\rm out}-1)+\Gamma_{\rm out}]}\right). \quad (13)$$

This fixes the pressure variation throughout both components. In the external medium, the thermal pressure is constant and set equal to the total pressure in the outer jet component. This is actually a slightly different value for cases (A), (B1) and (C), (D); albeit of the same order. The governing equation of state is taken as a Synge-type relation, also used in Meliani et al. (2004). As a result of the above profile prescriptions, the outer jet is relativistically cold with an effective polytropic index $\Gamma_{\rm eff} = 5/3$ and the inner jet has ultra-relativistic state $\Gamma_{\rm eff} = 4/3$. Case (B2) is an MHD variant to the hydro case with more stratified inner effective polytropic index already simulated in Meliani & Keppens (2007). The matter state between the two components is different (relativistically hot inner and cold outer jet), and we will see that during the time evolution, a shear region with an intermediate matter state forms. This variation in the matter state between various jet regions makes it vital to use a Synge–EOS to model growing instabilities and resulting turbulence. However, in the initial conditions of all cases, the polytropic index is relatively constant throughout each component. This is why we could use the polytropic EOS assumption to deduce a *near*-equilibrium solution of the initial two-component jet.

2.4. Dimensionless Characterization and Numerical Setup

As a result of the initializations described above, the local fast magnetosonic speed in the inner jet for case (D) and the local sound speed in the inner jet for cases (A) and (C) are of the order of 0.6 (light speed units), while cases (B1) and (B2) have a higher local fast magnetosonic speed. In the outer jet, the local fast magnetosonic speed of cases (C) and (D) and the local sound speed in cases (A) and (B2) are of the order of 0.2, while it is 0.07 in case (B1). Both inner and outer jets are kinetically dominated. The inner jet has an effective relativistic Mach number $M_{\rm fast} = \frac{\gamma\, V_p}{\gamma_{\rm fast}\, V_{\rm fast}}$ up to ∼40 for cases (A), (C), and (D), while the outer jet has $M_{\rm fast} \sim 14.0$ in cases (A), (B2), (C), and (D), and $M_{\rm fast} \sim 35$ in case (B1). However, both components are subsonically rotating, and during a complete rotation of the inner jet, the fast magnetosonic or sound wave will propagate about 200 times from the edge of the inner jet to the axis and back. Such overall configuration can easily develop non-axisymmetric instabilities, with growth times of order of the radial sound-crossing time (Hardee 2004).

The computational domain of this simulation is a 2D box of size -0.3 pc $< x <$ 0.3 pc and -0.3 pc $< y <$ 0.3 pc. The simulation is performed in Cartesian coordinates using an HLLC flux formula (Mignone & Bodo 2005). HLLC is a two state extension of the Harten, Lax, and van Leer flux formulation (HLL), which includes a proper representation for the contact wave. We use a piecewise parabolic method (PPM) limiter (Mignone et al. 2005). The combination of PPM reconstruction (third order accurate) and HLLC flux computations is extremely robust and handles both sharp discontinuities and turbulence development accurately. The lateral boundaries assume open boundary conditions, with a clipping of any inwardly directed momentum as soon as turbulent flow features start crossing the boundaries. The simulation is run till time $t = 50$, which due to our normalization translates to 163.2 year. The corresponding distance of jet propagation of the jet beam during this time is about 50 pc. The simulation is done using the AMRVAC code (Meliani et al. 2007; van der Holst & Keppens 2007; van der Holst et al. 2008) with a Synge-type equation of state. We take a base resolution of 120 × 120, allow for five grid levels, reaching an effective resolution of 1920^2. Shorter timescale runs at even higher resolutions were done to confirm that the dominant initial large-scale structure development is adequately resolved, although more fine scale features inevitably turn up. The simulations are performed typically using 120 processors for about two days per case. We add some white noise both at the initial time and at time $t = 1$ when various waves have already developed (this latter addition may not be essential to the evolution). The fact that we use Cartesian coordinates could give preference to instabilities with the mode number proportional to $m = 4$ character (the case studied in Meliani & Keppens (2007) was therefore confirmed separately in cylindrical coordinates, with the overall mode number dominance of $m = 4$ recovered). However, in all cases we study here, the instabilities dominating the dynamics and evolution of the jet have a clear mixture of many mode numbers.

3. RESULTS

In the actual simulations performed in this work, the magnetic field in the jet is taken purely poloidal. As explained before, our five simulations differ in their magnetic configuration: (A) is hydrodynamic; (B1) and (B2) have only the inner jet magnetized; (C) has only the outer jet magnetized, while in (D) both outflows are magnetized. This represents the main difference between the five cases, and while all cases will develop fairly complex nonlinear evolutions governed by multiple, interacting instabilities, our main aim is to determine which configuration can result in a clearly sustained two-component jet flow over a sufficiently long distance (time). It will turn out that cases (A), (C), and (D) all result in deceleration due to mixing between the two components, leading to decollimation of the jet, while only cases (B1) and (B2) convincingly maintain their two-component character. For later reference, important models parameters are listed in Table 1. We now continue to discuss the complex nonlinear evolution of the five cases in some detail.

Table 1
The Most Relevant Characteristics and Parameters for All Models Investigated

Case	Inner Jet		Outer Jet	Effective Inertia Ratio
	p_0	$B_{z,in}$(0.1375 Gauss)	$B_{z,out}$	$\gamma^2\rho h + B_z^2$ Ratio Out/In
A	2.3	0.0	0.0	0.15
B1	0.1	0.789	0.0	3.2
B2	10^{-4}	2.28	0.0	18.3
C	2.3	0.0	2.323	0.15
D	2	0.789	2.323	0.17

Notes. In addition to these tabulated values, the number density of the inner jet is fixed at 6.92×10^{-2} cm^{-3}, while $V_z = 0.99939c$ and $v_\varphi = 0.01c$. Constant values for the outer jet are number density 119.94 cm^{-3}, with $V_z = 0.9428c$ and $v_\varphi = 10^{-3}c$. The external medium is always static and unmagnetized, and has number density 10^{-2} cm^{-3}.

3.1. Case (A)

According to the Rayleigh criteria mentioned, the interface between the two components is always unstable. Also, the effective inertia of the inner jet is higher than in the outer jet. In fact, at the interface $R = R_{in}$, we have initially $(\gamma^2\rho h)_{out} \approx 0.07(\gamma^2\rho h)_{in}$. In Table 1, a $t = 0$ ratio is given using a value midway the outer jet divided by the axial value. The overall effective inertia contrast is very different from the case we investigated in Meliani & Keppens (2007), where the ratio between (mean value of) effective inertia of the inner component jet to the effective inertia of the outer component jet was such that $(\gamma^2\rho h)_{out} \gg (\gamma^2\rho h)_{in}$.

Initially, a linear surface mode develops at this interface $R = R_{in}$. As a direct consequence, a small, radially extended the shear region with low effective inertia $\gamma^2\rho h$ forms at this location. At both bounding interfaces of this small shear layer, one with the outer and one with the inner jets, small wavelength instabilities develop. Meanwhile, acoustic waves from the inner interface propagate inward reflect on the jet axis, and then give rise to a Kelvin–Helmholtz-like body mode with a dominant azimuthal mode number $m \sim 8$ in the inner jet. Meanwhile, the surface instability at the interface between inner jet and shear shell reaches a clearly nonlinear phase. The overall interaction then gives rise to the growth of a relativistically enhanced Rayleigh–Taylor-type instability, having a body mode character propagating into the inner jet (Figure 2, top). This instability regime shows about four arms at first that collapse to three arms which progressively propagate inward. As will be detailed later on, this instability can be explained from the fact that in this case (A), fluid elements in the shear layer have a lower effective inertia $\gamma^2\rho h$ and higher pressure than pre-existing material in the inner jet.

We could qualitatively describe this relativistic Rayleigh–Taylor instability as follows. A fluid element in the shear layer is at first typically rotating with a speed of order of $V_\varphi \sim 0.01$, the initial rotation speed at the inbound interface. The lower inertia of the shear shell relative to the inner jet makes that transfer of angular momentum from the inner wind/jet region to the shear layer is rather efficient, causing a fast rotational speedup of the shear layer matter. At the same time, the centrifugal force acting on a fluid element moving inward varies with $1/R$. Because the fluid inertia in the shear region ends up at about a 12 times lower value than the inertia in the inner jet, the centrifugal force acting on this fluid element is much weaker than in the inner wind. At the same time, the pressure in the shear layer fluid element is higher than in the inner wind. Therefore, the element

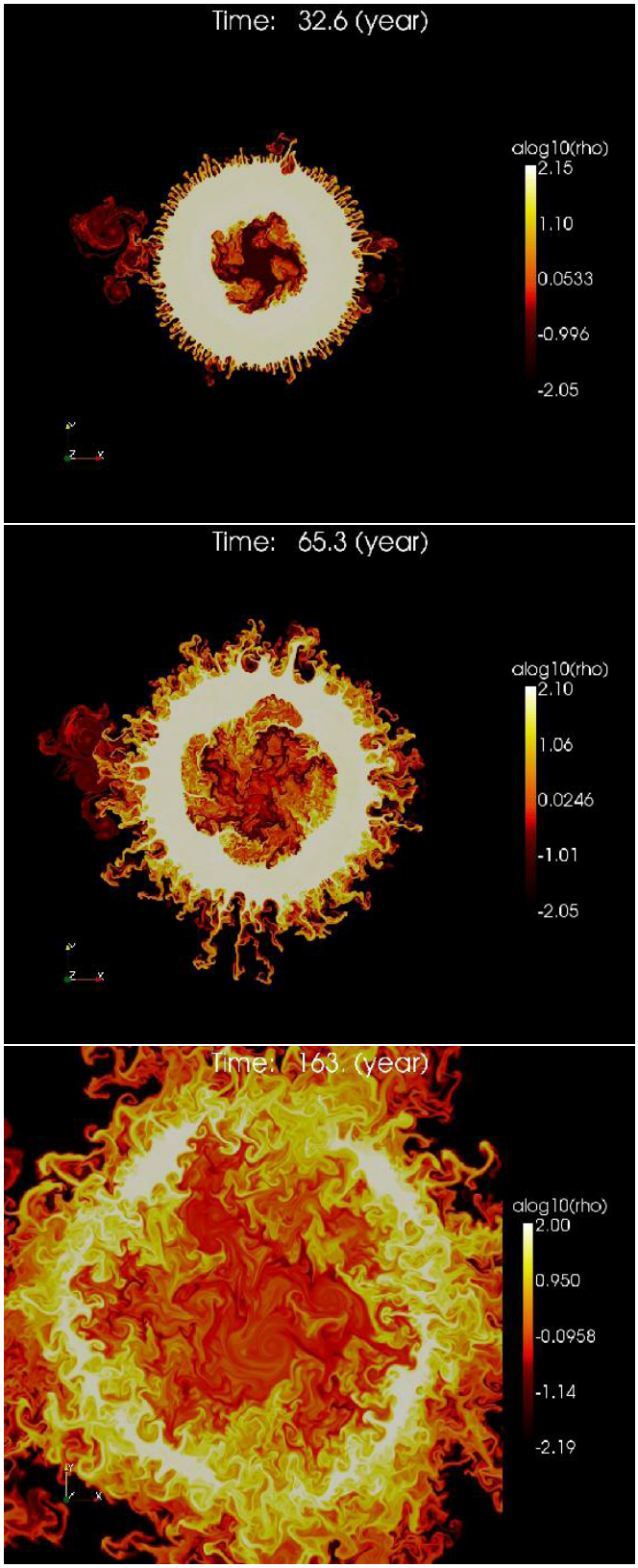

Figure 2. Case (A), the purely hydrodynamical jet, showing logarithm of proper density at times (top) $t = 32.6$ year: development of relativistically enhanced Rayleigh–Taylor-type instability propagating inward in the inner jet, (center) $t = 65.3$ year: merging of the three Rayleigh–Taylor fingers at the jet axis and (down) $t = 163$ year: decollimation of the jet (one full rotation of the inner jet corresponds to $t = 65.3$ year).

(A color version of this figure is available in the online journal.)

will expand inward until the pressure gradient gets balanced by the centrifugal force. In this particular simulation, three prominent fingers form and start propagating inward. However, as the initial pressure profile decreases toward the jet axis, the centrifugal force in the inner jet decreases inward. With such a configuration, we find that in the phase where the intruding, rotating fingers of the Rayleigh–Taylor mode propagate inward, they will nearly reach the jet axis. Very close to the axis, the centrifugal force acting on them gets compensated by the pressure force. In the phase that follows, the rotating fingers get deflected sideways in the direction of rotation. After less than half a full rotation of the inner jet (at $t \sim 32.6$ year, see Figure 2, top), this relativistic Rayleigh–Taylor mode then dominates the body mode instability in the inner jet. The Rayleigh–Taylor fingers propagating inward also compress the inner jet. Since angular momentum is conserved, the centrifugal force increases, and the inner jet fluid moves outward toward the shear shell. This means that we get enhanced angular momentum transfer from the inner jet to the shear layer shell, which accelerates the rotational speed of the shear shell. We find that after less than one total rotation of the inner jet (at $t \sim 65.3$ year, see Figure 2, center), the three Rayleigh–Taylor fingers nearly merge, making the inner jet appearance totally dominated by the (growing) shear shell.

An analysis of this relativistic Rayleigh–Taylor-type instability is described separately in Section 4. The low effective inertia of fluid in the shear region makes the interface between the shear flow and the inner jet unstable to this instability, where centrifugal forces act as an effective (radially outward pointing) gravity. Once initiated, these grow faster than the previously formed Kelvin–Helmholtz body mode. A number of "arms" develop from the shear region, having lower angular momentum than the fluid from the inner region, propagate inward, while inner jet fluid having higher angular momentum propagates outward. The end result is transfer of energy and angular momentum from the inner jet to the growing shear region. As a consequence of this complex mixing of jet and shear layer matter, we find significant deceleration of the inner jet, while the density and radius of the inner jet plus shear region increase (this is quantified later in Figure 8).

The external boundary of the growing shear region at $R \approx R_{\rm in}$ which borders the outer cold jet is also Kelvin–Helmholtz unstable. For the case at hand, in a first phase, a larger scale Kelvin–Helmholtz-type mode develops with eight undulations initially, eventually converging to form about five large-scale structures (see Figure 2, center). This is different from the case studied before in Meliani & Keppens (2007), where the most prominent feature in the nonlinear evolution was the development of a Kelvin–Helmholtz-type mode with four arms. This mode transfers angular momentum from the shear region to the outer jet and decollimates the jet. At smaller spatial scale, but also at the interface between the shear region and the outer jet, other instabilities develop as well. These are again more centrifugally driven, as angular momentum and pressure increase in the shear region. Thus also at this interface, the centrifugal force becomes locally higher than in the outer outflow. Small bubble-like protrusions from the shear shell enter the outer outflow. However, since the pressure of the outer jet slowly increases outward, the growth of this smaller scale instability is stopped when the centrifugal force of the protruding bubbles gets balanced by the pressure of the outer jet. Therefore, this instability remains weak and the large-scale dynamics of the interaction between the shear layer and the outer jet remains dominated by the Kelvin–Helmholtz instability. The small scale instabilities do influence the dynamics by increasing the efficiency of the angular momentum transfer from the Kelvin–Helmholtz structures to the outer jet. Finally, also the outer interface at $R \approx R_{\rm out}$ between outer jet and the hot, dilute medium is Rayleigh–Taylor unstable, and is dominated by small wavelength perturbations.

As the overall outcome of all the interacting instabilities, the two-component jet decollimates, such that the jet radius increases to $R_{\rm out} \sim 0.28$ pc (see Figure 9). The inner component jet also spreads and its radius reaches $R \sim 0.18$ pc (see Figure 8). Also during the simulated 163 years in physical time (Figure 2, down), the rotation speed of both components decreases, and the interaction between the shear region and the outer component is dominated by Kelvin–Helmholtz-induced behavior, together with the relativistically enhanced Rayleigh–Taylor instability of the inner rotating fluid. The main result of this interaction between the two components is the dramatic deceleration of the inner jet. In fact, the relativistic Rayleigh–Taylor-type instability leads to a deceleration of the inner component where the Lorentz factor of the inner component drops to $\gamma \sim 8$ (quantified later for all models in Figure 7).

3.2. Cases (B1) and (B2)

We now describe the two-component jet evolution with a magnetized inner component. The effective inertia in the inner jet is lower than in the outer jet with initial contrasts $(\gamma^2 \rho\, h)_{\rm out} \approx 3.2(\gamma^2 \rho\, h + B_z^2)_{\rm in}$ in case (B1) and $(\gamma^2 \rho\, h)_{\rm out} \approx 18(\gamma^2 \rho\, h + B_z^2)_{\rm in}$ in case (B2), due to the initial lower pressure at the jet axis and the initial different distribution over thermal and magnetic energy in them. These cases are then such that the inner interface is now stable against the dominating Rayleigh–Taylor-type instability described above and explained analytically in Section 4. Still the interface at $R \approx R_{\rm in}$ between the inner and outer jets is subject to Kelvin–Helmholtz instability because of the differential rotation. This modifies the shape of the interface surface, leading to non-axisymmetric reflection of MHD waves propagating through the inner jet. These waves in turn disturb locally the initial equilibrium between total pressure gradient and centrifugal force.

During the evolution, some spikes develop at the interface, where the outer jet locally interchanges with the inner jet. These spikes are accelerated in the toroidal direction by the faster rotating inner jet. The centrifugal force acting on these slows down their inward expansion, and they then mainly propagate in the toroidal direction. Their interaction with the inner jet material induces Kelvin–Helmholtz body mode instability, with a spiral pattern forming, this time having 3 arms in the two cases (see Figures 3, top and 4, top). They extract some angular momentum from the outer regions of the inner jet, slowing its rotation. Again, a shear shell then forms in this region, continuously extracting angular momentum from the inner jet/wind. The spikes then slowly expand to the jet axis. The inner wind gets compressed by the shear layer. However, these mainly Kelvin–Helmholtz-type instabilities turn out to have lower efficiency in extracting angular momentum than the relativistic Rayleigh–Taylor instability encountered in case (A). The compression of the inner jet by the shear region is followed by a modest expansion. In case (B2), the extraction of the angular momentum is weaker than that in case (B1), because in case (B2), the inner jet has lower inertia. Meanwhile, the angular momentum extracted from the inner jet leads to an outward extension of the shear shell that formed at $R_{\rm in}$. At the

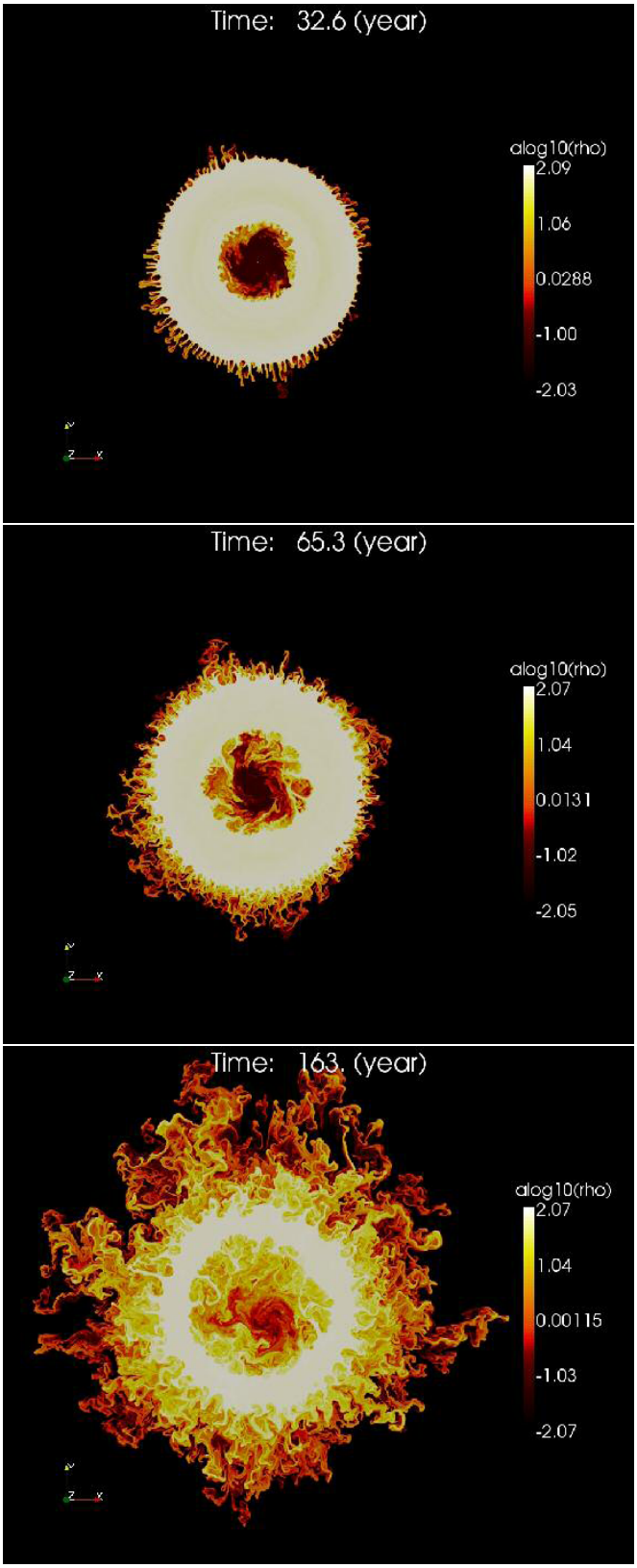

Figure 3. Case (B1), only the inner jet is magnetized. Logarithm of density at (top) $t = 32.6$ year: development of Kelvin–Helmholtz body mode instability at the interface between the inner and outer jets, (center) $t = 65.3$ year: inward growing of the shear shell in the inner jet and (down) $t = 163$ year: development of Rayleigh–Taylor at the outer jet interface, with one rotation of the inner jet completed at $t = 65.3$ year.

(A color version of this figure is available in the online journal.)

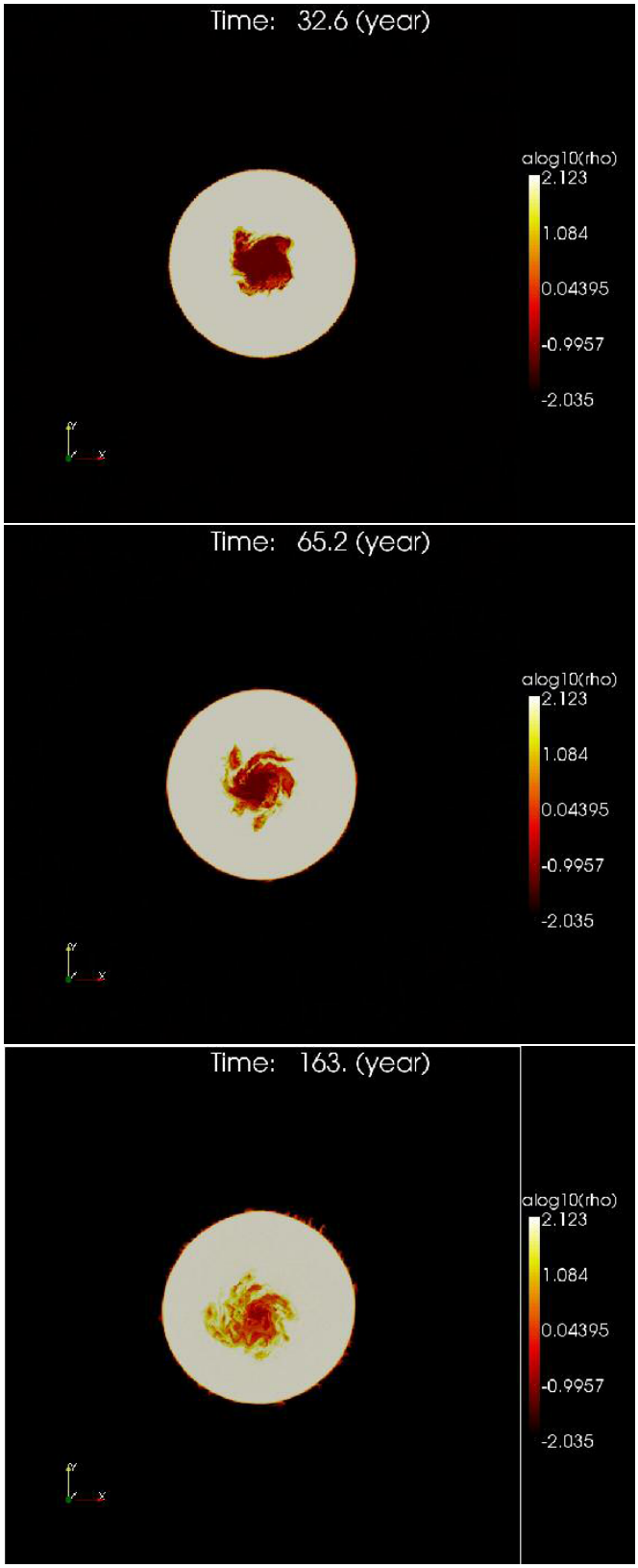

Figure 4. Case (B2), only the inner jet is magnetized. Logarithm of density at (top) $t = 32.6$ year: development of Kelvin–Helmholtz body mode instability at the interface between the inner and outer jets, (center) $t = 65.3$ year and (down) $t = 163$ year: the inner jet component is deplaced from its on-axis position due to significant non-axisymmetric mode development, with one rotation of the inner jet completed at $t = 65.3$ year.

(A color version of this figure is available in the online journal.)

interface between this growing shear shell and the outer jet, a Kelvin–Helmholtz instability surface mode with the azimuthal mode number $m \sim 3$ character then develops. Also at this interface, smaller scale Rayleigh–Taylor instability proceeds. The shear shell has an effective inertia which is lower than the outer jet inertia. As locally centrifugal forces dominate, low inertia "bubbles" radially extend toward the outer jet. The growth rate of these bubbles is rather slow, since the pressure of the outer jet increases mildly outward, and the slowly rotating outer jet breaks their rotation.

At the outer surface $R_{\rm out}$ of the outer jet in case (B1) (see Figure 3), we also witness Rayleigh–Taylor instability, as in case (A). On the other hand, case (B2) shows little evidence for such instability at the outer jet surface (see Figure 4), which is due to the different external pressure conditions there. Throughout the simulation, the jet in (B1) and (B2) remains collimated by the outer component, which compresses the inner component and shear region. The inner component jet radius in case (B1) at 163 years remains lower than 0.07 pc and in case (B2) even below about 0.04 pc (see Figure 8). However, in case (B1), the Rayleigh–Taylor instability at the surface of the outer region forms an extended sheet, which gives an increase to the apparent total jet radius $R_{\rm jet} = 0.2$ pc (see Figure 9), whereas the jet in case (B2) does not show any sign of decollimation.

Both the inner jet and the shear region end up magnetized. The main difference between these cases and all others studied here is that despite all small-scale instability development, the inner jet decelerates little, dropping to an average Lorentz factor of about 20 (see Figure 7). The two-component jets for cases (B1) and (B2) remain clearly separable in inner and outer jet components (see Figures 3, down-4, down), which is not the case for all other evolutions shown here. In both cases (B1) and (B2), we do find that the inner jet component is deplaced from its on-axis position due to significant non-axisymmetric mode development. The jet stratification converges to a structure with an inner fast, magnetized spine having a Lorentz factor of about 20. The spine is surrounded by a shear shell being 100 denser than the spine and with a lower Lorentz factor and low magnetization. The difference between the two cases is that the high magnetic pressure and low thermal pressure in the inner jet for case (B2) increase its nonlinear stability as compared to case (B1).

3.3. Case (C)

In this case, only the outer jet is magnetized with a purely poloidal magnetic field. As mentioned before, the rotation of the jet is subsonic, such that acoustic waves which start to propagate from the inner–outer jet interface at different stages in the evolution propagate inward and are reflected about 200 times during one rotation period of the inner jet. Our simulations follow about 2.5 full inner jet rotations. As the interface between the two components is unstable to various mode types as already encountered in the previous cases, its shape changes and the acoustic wave propagation becomes strongly non-axisymmetric. These waves play a clear role in disturbing the initial axisymmetry of the inner jet, and mitigate the development of non-axisymmetric body mode instabilities in the inner jet.

In this case (C), in a first stage, linear small-wavelength (compared to case (A)) Kelvin–Helmholtz instabilities develop at the interface $R \approx R_{\rm in}$ between the two components. These reach a nonlinear phase in less than a tenth of a full rotation. Spikes of the outer jet, which are this time magnetized, arise in the inner jet. The large ratio of the fluid inertia between the outer and inner jet makes these spikes once more unstable to the centrifugally mediated, relativistically enhanced Rayleigh–Taylor instability seen previously in case (A). This gives rise to the formation of rotating "bubbles" that protrude inward. In the case at hand, about 10 such bubbles form (see Figure 5, top), having smaller size compared to those seen to emerge in case (A). This difference results due to the difference in the Kelvin–Helmholtz surface mode development mentioned earlier. The initial smaller size of the protruding bubbles makes their growth rate slower than in the purely hydrodynamical case (A), until they reach the merging phase where in this case about three larger size bubbles form and converge to the jet axis. Meanwhile, these bubbles compress and push fluid elements from the inner jet to a shear layer (see Figure 5, center). Thus once again, the larger-scale mode structures act to transfer angular momentum from the inner jet to the shear region.

Since the bubbles which move radially inward form at the shear shell, their ratio of magnetic pressure to thermal pressure $B_z^2(1 - V_\varphi^2)/(2\,p) \sim 0.1$ is lower than in the outer jet. In fact, the shear region is made up of fluid from the inner and outer jets, and its thermal pressure dominates total pressure. The external surface of the shear shell is Kelvin–Helmholtz unstable and about six arms form (see Figure 5, center). From each one, a centrifugally driven spike propagates outward. In fact, angular momentum extracted from the inner jet in the end gets transferred to the external part of the shear region. Then, locally the centrifugal force at the interface between the shear shell and the outer jet acts to develop spikes which decollimate the jet (see Figure 5, down). The total jet radius increases from 0.1 pc at the initial stage to 0.189 pc (Figure 9), after the jet has propagated for a distance of 50 pc. In the same time, the inner jet spreads as well, decelerates, and its Lorentz factor drops to about 8. At the end state, the jet is constituted of an inner turbulent component with a radius of 0.15 pc (see Figure 8) and a small outer component. The final rotation speed profile increases from the axis to 0.006 at 0.04 pc, further decreasing outward.

3.4. Case (D)

In this last case, both inner and outer jets are magnetized. Initially, from the discontinuity between the two components, fast magnetosonic waves propagate both outward into the outer jet, and inward into the inner jet. The end result of the initial re-adjustment is that a small shear region with lower magnetization than both component develops at the interface $R \approx R_{\rm in}$. Also this configuration is Kelvin–Helmholtz unstable. At the surface from the shear region, roughly 13 bubbles arise, moving inward into the inner jet (see Figure 6, top). They merge to form three large arms expanding toward the jet axis (see Figure 6, center). Fluid from the inner jet is pushed outward, thereby extracting angular momentum from the inner jet. Since the structures form at the shear region, the magnetic pressure inside the bubbles is lower than in the inner and outer components. However, the thermal pressure is increased in the shear region. During the evolution, dominant forces are magnetic pressure and thermal pressure that balance each other, while the contribution of the centrifugal force is low. However, the centrifugal force remains responsible for triggering instabilities. As in case (C), the shear region grows with eventual almost complete destruction of the inner jet component (see Figure 6, center). In the last phase simulated, the dominating inner shear region becomes totally turbulent, and strong vortices form, changing the full jet shape

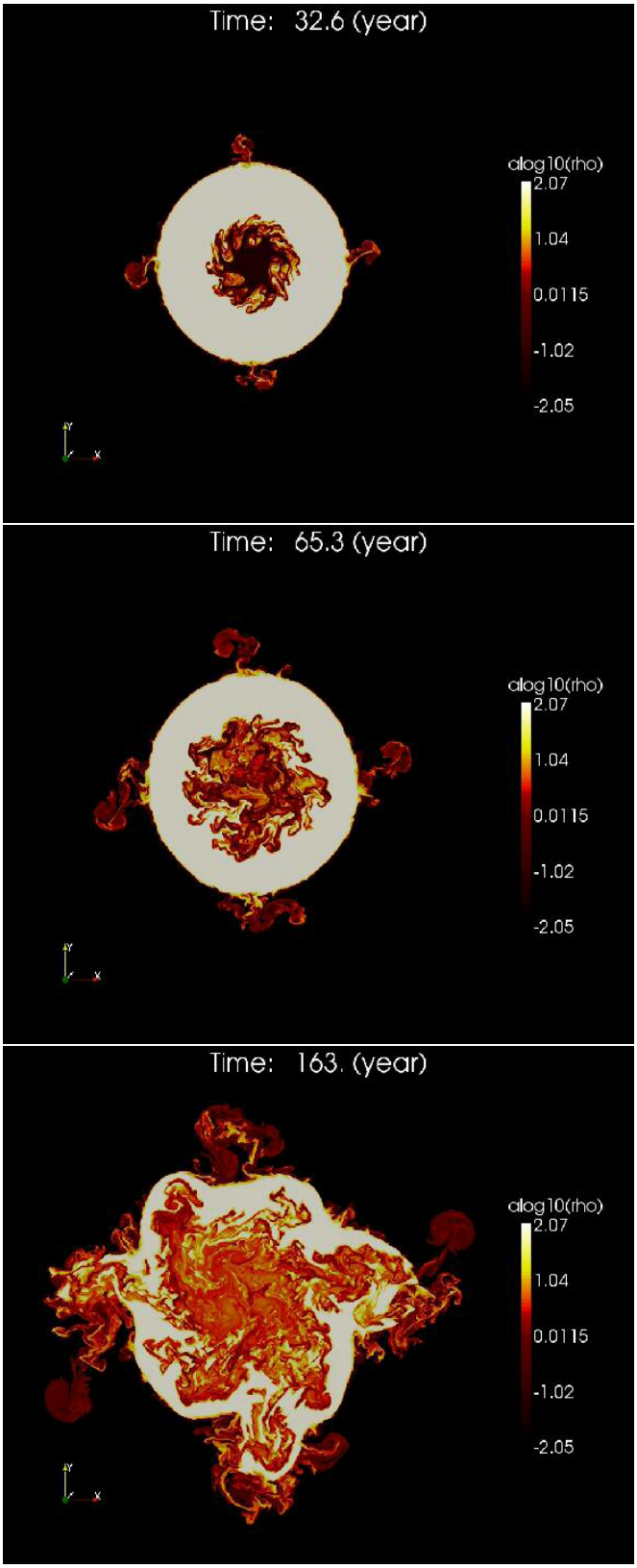

Figure 5. Case (C), only the outer jet is magnetized. Logarithm of density at (top) $t = 32.6$ year: Rayleigh–Taylor instability develops at an interface between the two component inducing rotating "bubbles" that protrude inward, (center) $t = 65.3$ year: "buabbles" merge at the jet axis and inner jet decelerates and becomes turbulent and (down) $t = 163$ year: The shear shell expand outward in the outer jet and decollimates the jet, with one full inner jet rotation at $t = 65.3$ year.

(A color version of this figure is available in the online journal.)

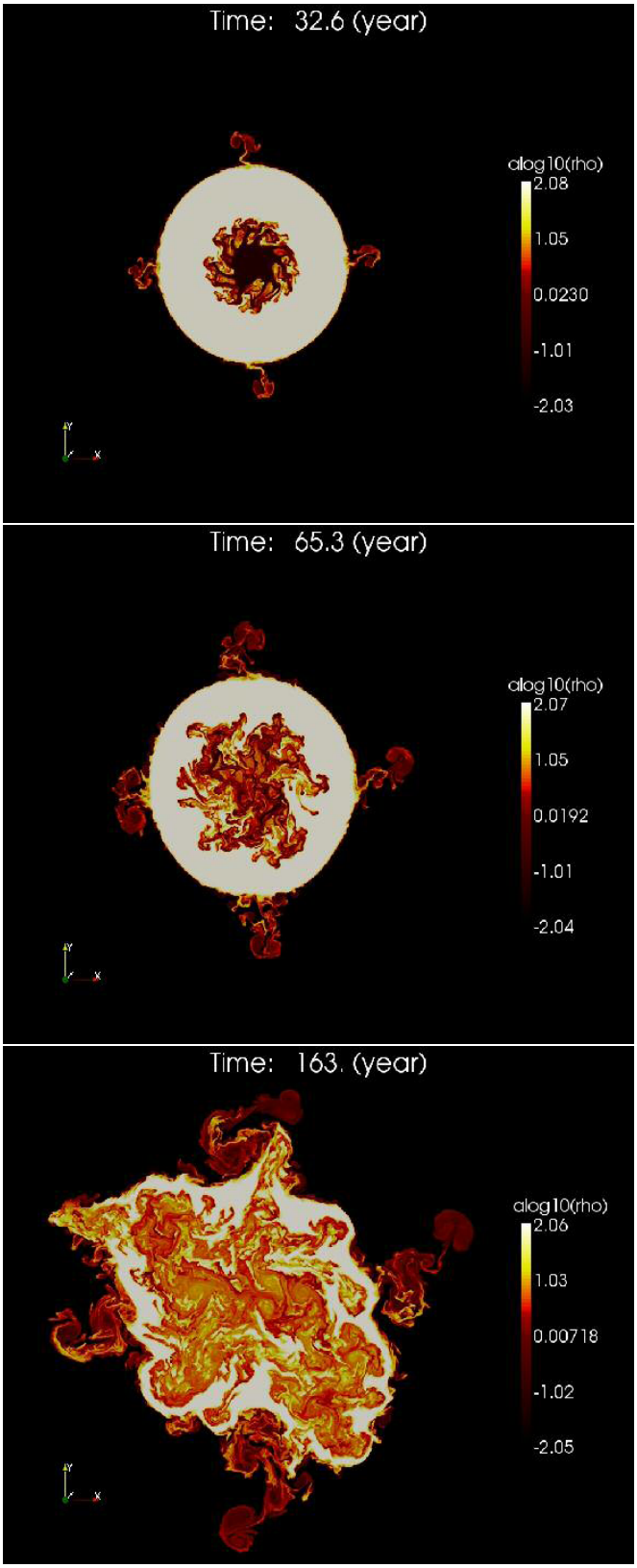

Figure 6. Case (D), both jet components magnetized. Logarithm of density at (top) $t = 32.6$ year: 13 bubbles arise, moving inward into the inner jet, (center) $t = 65.3$ year: Rayleigh–Taylor bubbles emerge at the jet axis, and the inner jet becomes turbulent and (down) $t = 163$ year: The shear region grows and changes the full jet shape to elliptic, with one full rotation of the inner jet corresponding to $t = 65.3$ year.

(A color version of this figure is available in the online journal.)

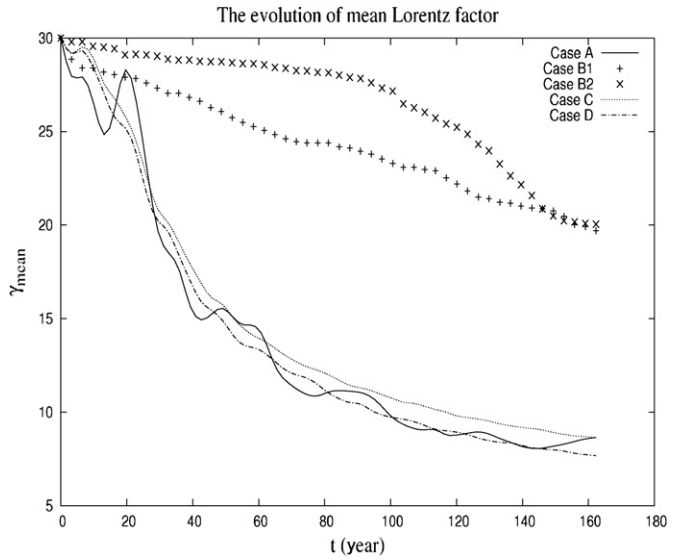

Figure 7. Time evolution of the mean Lorentz factor of the inner jet in the five cases. For the cases (A), (C), and (D), we distinguish between the inner and outer jets according to the polytropic index and Lorentz factor. In cases (B1) and (B2), we use the same condition for the Lorentz factor to distinguish between the inner and outer jets, as well as the extra condition that the inner jet is magnetized.

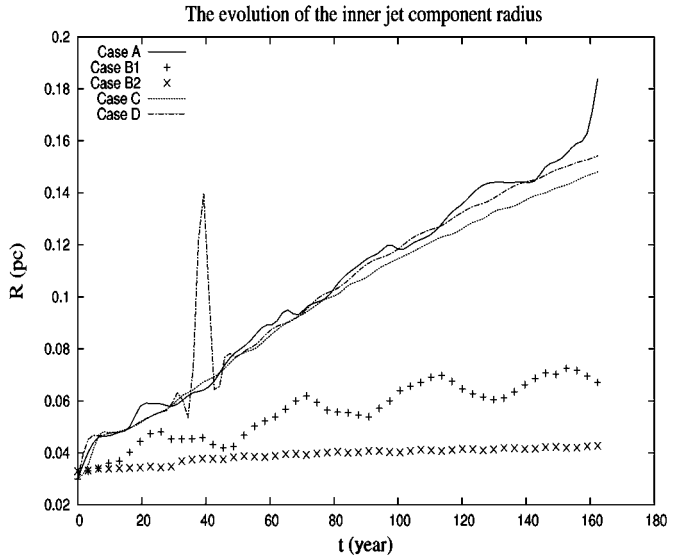

Figure 8. Time evolution of the effective inner jet radius in all cases. For cases (A), (C), and (D), we distinguish between the inner and outer jets according to the polytropic index and Lorentz factor. For cases (B1) and (B2), we use the same condition for the Lorentz factor and the condition that the inner and shear components are magnetized. The effective inner jet radius is $\sqrt{S_{\rm in}/\pi}$, where $S_{\rm in}$ is the surface thus found for the inner jet. The jets (B1, B2) with low inner kinetic energy flux contribution are more stable and remain relativistic and the jets (A, C, D) with high inner kinetic energy flux contribution are unstable and decelerate.

to elliptic (Figure 6, down). At this phase, the average Lorentz factor of the inner jet has dropped down to $\gamma_{\rm max} \sim 7$ (see Figure 7).

4. RELATIVISTICALLY ENHANCED RAYLEIGH-TAYLOR

In cases (A), (C), and (D), a relativistic, Rayleigh–Taylor-type instability developed. Here, we first describe in a qualitative way how this instability ensues, and then continue to explain it using an approximate linearization.

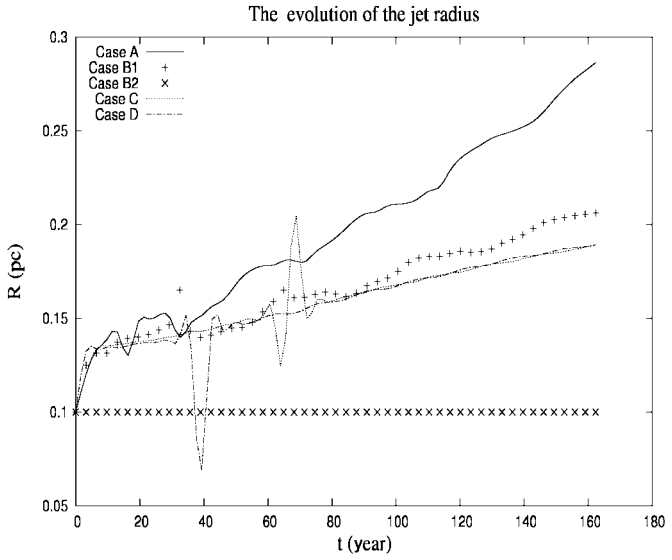

Figure 9. Time evolution of the effective jet radius in all cases. The effective jet radius is $\sqrt{S_{\rm jet}/\pi}$, where $S_{\rm jet}$ is the surface occupied by the full (inner+outer) jet. The jets (A, C, D) with high inner kinetic energy flux contribution decollimate.

At the interface between the two outflow components, we mentioned that (linear and then nonlinear) surface modes develop, due to velocity shear hence of Kelvin–Helmholtz type. Fluid of lower inertia (low $\gamma^2 \rho h$) and higher pressure then penetrates the inner jet. Since the inertia in the penetrating spikes is lower than in the surrounding inner jet material, the centrifugal force acting on these is weaker. The spikes then expand inward until the pressure is balanced by the centrifugal force. They expand sideways as well, again on the basis of pressure balance and ram pressure arguments. Due to the big difference in inertia, transfer of angular momentum from the inner jet to these inward penetrating spikes is very efficient. Rather quickly then, their rotation speed reaches the rotation speed of the inner jet at the initial interface, set by $v_{\varphi,\rm in}$. During its further inward expansion, this rotation speed remains constant. However, the low inertia of the spikes keeps their angular momentum lower than the inner jet matter.

To explain this phenomenon semi-analytically, we confine our attention to a perturbation depending only on the radial direction R. Let $dR = \tilde{v}_{\rm R} dt$ represent the radial displacement of the contact surface between the two components during dt, and $\tilde{v}_{\rm R}$ the perturbation speed. The momentum equation governing the fluid near our initial equilibrium writes as

$$\left(\gamma^2 \rho h + B_z^2\right)\left[\frac{\partial}{\partial t} + \vec{V}\cdot\nabla\right]\vec{V} + \nabla p_{\rm total} + \vec{V}\frac{\partial p_{\rm total}}{\partial t} + \cdots = 0, \quad (14)$$

with $p_{\rm total} = p + \frac{B^2}{2}$. In this equation, we already ignored the lab frame contribution of the charge separation, which is justified for rotational flows far within the light cylinder, as is the case in our model here.[4] Moreover, the magnetic topology taken here does

[4] Note that we mentioned a jet radius of 0.1 pc at a distance of 1 pc for M87. The estimated light cylinder radius for M87 is smaller than 0.1 pc if a large fraction of the angular momentum (then Poynting flux) extracted from the accretion by the magnetic field is transferred to the stream lines during the acceleration phase by the ideal RMHD mechanisms (Begelman & Li 1994). But in our model, we assume that the jet is accelerated also by non-ideal RMHD mechanisms with decay of the toroidal magnetic field by dissipation/reconnection, leading to a fast central spine jet, and overall low rotation profiles (weak transfer of angular momentum from magnetic fields to stream lines).

not involve magnetic pinching; hence, magnetic effects only add to the total pressure and to the effective inertia, where also $V_\varphi \ll V_z$ is used. Then the radial component of Equation (14) can be further approximated, if we neglect temporal variation of the total pressure and use $\frac{\partial \tilde{v}_R}{\partial \varphi} = 0$, to get

$$\left(\gamma^2 \rho h + B_z^2\right)\left[\frac{\partial \tilde{v}_R}{\partial t} - \frac{V_\varphi^2}{R}\right] + \frac{\partial p_{\rm total}}{\partial R} = 0. \qquad (15)$$

According to the initial condition, the inertia $\gamma^2 \rho h$ of the fluid varies slowly in the inner and outer jets. We can thus argue that both inertia and toroidal speed in each fluid element vary slowly when it undergoes a small radial displacement $\zeta = R_{\rm in} - R = \int \tilde{v}_\zeta dt = -\int \tilde{v}_R dt$ from the initial interface position $R_{\rm in}$, with $|\zeta| \ll R_{\rm in}$. Using the main equilibrium balance between centrifugal force and total pressure gradient, the variation of the total pressure can be argued to lead to

$$\tilde{p}_{\rm total} = \left(\gamma^2 \rho h + B_z^2\right)\left[\frac{\partial \int \tilde{v}_\zeta d\zeta}{\partial t} + \frac{V_\varphi^2 \zeta}{R_{\rm in}}\right]. \qquad (16)$$

To get an approximate dispersion relation, we assume that to first order, the perturbation speed is potential, i.e. $\tilde{v}_\zeta = (\nabla \Psi)_\zeta$ and that we have $\Psi \propto \exp(\lambda t - k|\zeta|)$. Noting that the displacement $\zeta = \int \tilde{v}_\zeta dt$ must be identical for inner/outer regions, and using total pressure and displacement continuity arguments, we then get the essential proportionality relation between the instability growth rate and wave number

$$\lambda^2 \propto k\left[\left(\gamma^2 \rho h + B_z^2\right)_{\rm in} - \left(\gamma^2 \rho h + B_z^2\right)_{\rm out}\right]. \qquad (17)$$

This approximative dispersion relation indicates that for two-component stability, we need $\lambda^2 < 0$ requiring that $(\gamma^2 \rho h + B_z^2)_{\rm out} > (\gamma^2 \rho h + B_z^2)_{\rm in}$. This confirms that the interface between the two rotating components is stable against a centrifugally driven, relativistic Rayleigh–Taylor instability, when the effective inertia of the outer component is higher than the effective inertia of the inner component. This important result correlates well with the results of all simulations in Section 3 as well as in our previous publication (Meliani & Keppens 2007). In fact, this equation explains why cases (A), (C), and (D) are relativistically Rayleigh–Taylor unstable since we find typical contrasts during the evolution in (A) $\left(\gamma^2 \rho h + B_z^2\right)_{\rm out} \approx 0.75\left(\gamma^2 \rho h + B_z^2\right)_{\rm in}$, in (C) and (D) $\left(\gamma^2 \rho h + B_z^2\right)_{\rm out} \approx 0.1\left(\gamma^2 \rho h + B_z^2\right)_{\rm in}$, whereas cases (B1) and (B2) are relativistically Rayleigh–Taylor stable since $\left(\gamma^2 \rho h + B_z^2\right)_{\rm out} \sim 10\left(\gamma^2 \rho h + B_z^2\right)_{\rm in}$ in (B1) and $\left(\gamma^2 \rho h + B_z^2\right)_{\rm out} \sim 20\left(\gamma^2 \rho h + B_z^2\right)_{\rm in}$ in (B2). Initial effective inertia ratios derived from the initial conditions are mentioned in Table 1, and it is clear that we can set up stable versus unstable cases by varying the contrast of effective inertia between inner versus outer jets. This also works in pure hydro, and indeed the pure hydro case from Meliani & Keppens (2007) does not suffer from this newly discovered instability. For the purely poloidal field configurations studied here, magnetic field effects are prominent in total pressure and effective inertia alone. Note finally that it is a truly relativistic effect, since the same argument in classical MHD just involves the density difference between outer versus inner jet. Under the conditions of a light inner jet with heavy outer jet taken here, a classical variant of relation (Equation (17)) involves only $\rho_{\rm out} - \rho_{\rm in}$ and would predict stability.

5. DISCUSSION AND CONCLUSIONS

We examined five configurations of magnetized two-component jets. All share the same density ratio between inner and outer components and identical rotation profiles. The magnetic and thermal pressure configuration in each model differs, though. This in turn translates to different distributions of the (total, fixed) kinetic energy flux over the inner and outer jet components. In fact, in case (A), the kinetic energy flux in the inner component is about 10%, while it is 0.7% for case (B1) and 0.5% in case (B2), and around 38% for cases (C) and (D). For the outer component, we thus have 90% in case (A), 99.3% in case (B1) and 99.5% in case (B2), and only 62% for cases (C) and (D). The most important difference between the two model categories is then: cases (A, C, D) have an inner jet component with higher inertia $\gamma^2 \rho h + B_z^2$ than their outer jet component, while cases (B1) and (B2) have an inner jet component inertia which ends up lower than in the outer jet component. From the detailed analysis of the simulations, as well as from the approximate stability analysis, this criterion distinguishes between cases where relativistically enhanced Rayleigh–Taylor modes ultimately dominate the evolution, leading to complete mixing of both components and inner jet deceleration. This is quantified most clearly by showing the time evolution of the mean Lorentz factor over the inner jet region for all cases in Figure 7. This requires a clear criterion to distinguish inner versus outer jets in the turbulent evolutions. In cases (A), (C), and (D), we locate the outer jet component as having a Lorentz factor $2.5 < \gamma < 3.5$ and effective polytropic index $\Gamma_{\rm eff} > 3/2$. The inner component is the region defined by a Lorentz factor $\gamma \geqslant 3.5$ and effective polytropic index $\Gamma_{\rm eff} \leqslant 3/2$. In cases (B1) and (B2), the effective polytropic index in the inner and outer jets can be locally of the same order there; hence, we use that the inner jet is magnetized. In cases (B1) and (B2), the inner component jet and shear region are not totally mixed during the evolution, since the inner component is compressed and has higher magnetization and Lorentz factor. Thus to distinguish the inner component jet, we put a condition on magnetic field strength $B_z > B_{z,\rm initial}/2$, where $B_{z,\rm initial}$ is the magnetic strength assumed initially. Under these precise quantifications of inner/outer jet regions, Figure 7 demonstrates clearly that how stable cases (for the relativistically enhanced Rayleigh–Taylor modes) remain at high speed, while unstable cases decelerate. Using the same means to distinguish inner versus outer jet regions at all times, we can quantify the inner jet radius for all cases, as well as the total jet radius for all cases. These are shown in Figures 8 and 9, and quantify the decollimation effects discussed in Section 3.

During the entire evolutions, the toroidal and radial speeds remain weak as we have typically a maximal $V_R < 0.01$ and $V_\varphi < 0.04$. This means that the contribution of the laboratory frame charge separation force $\rho_e \vec{E}$ to the Lorentz force is negligible at all times. Under these conditions, in both radial and toroidal directions, the contribution of magnetic energy to fluid inertia is $1/\gamma^2$ weaker than the contribution of the magnetic pressure to the total pressure. This explains why cases (B1) and (B2) are then more stable than the other cases. Despite the fact that case (B2) has similar axial total pressure than other cases (A, C, D), the low contribution of thermal energy to total pressure makes the effective inertia ratio between the inner and outer jets low. This two-component jet is then stable against the relativistically enhanced Rayleigh–Taylor instability. Extraction of angular momentum and energy from the inner jet to the shear

shell is less efficient in cases (B1) and (B2) than in all other cases. As a result, in cases (B1) and (B2) the inner relativistic jet with a high Lorentz factor $\gamma_{\rm in} \sim 20$ persists. In other cases, the kinetic energy flux in the inner jet was initially relatively high, making them unstable and leading to deceleration to Lorentz factors around 8.

We investigated the stability of two-component jets beyond the launching region, where both components are rotating differently and a clear two-component structure exists. We initialized this model in accord with magnetocentrifugal models for jet generation, also using the observed analogy between radio source jets and two-component jets in young stellar objects, where the rotation within the jet can actually be observed. We performed five very high-resolution simulations of magnetized two-component jets with various magnetization and kinetic energy flux stratifications. The two-component jets with a low inner kinetic energy flux contribution are more stable and remain relativistic for long distances, whereas jets with a highly contributing inner jet to the total jet kinetic energy flux are subject to a relativistic Rayleigh–Taylor-type instability. This instability turns out to be very efficient to decollimate and decelerate the inner jet. Jets that are subject to this instability become turbulent after propagating for a distance of about 30 pc.

This new result on two-component jet models is important because it can explain the classification of radio sources in Fanaroff–Riley I/II categories according to the energy stratification of the inner jet. This ultimately relates to the jet launch region and the properties of the inner accretion disk. In fact, by analogy between the FRI/FRII classification and the results of our model, an FRI jet would correspond to a two-component jet with a high energy flux contribution from the inner jet, whereas the FRII jet corresponds to relatively low energy fluxes in the inner jet. The model we propose here to explain the FRI/FRII dichotomy is different from the model we proposed earlier (Meliani et al. 2008) where the transition occurs due to external density stratification. That model explains the group of peculiar "HYbrid MOrphology Radio Source" (HYMORS; Gopal-Krishna & Wiita 2000) which appear to have an FRII type on one side and an FRI-type diffuse radio lobe on the other side of the active nucleus. Since the launch conditions on each side are presumably similar in these kind of radio sources, the different Fanaroff–Riley morphologies on either side must be attributed to the change in the properties of the ambient media, as shown convincingly in Meliani et al. (2008). The results of the present paper nicely complement these earlier findings with a quantifiable role of the central engine contribution.

We currently continue this study of the interaction between two component jets in full 3D. We thereby intend to explore the relative influence of azimuthal versus longitudinal instabilities for realistic multi-component jets. Another extension is to allow for aximuthal magnetic fields in accord with the initial profiles as given generally in this paper. It then remains to be shown that (1) the newly discovered instability persists in 3D hydro and MHD configurations, where the potential role of axial mode development is incorporated, and introduces helical jet axis displacements; (2) how the instability gets modified (stabilized or destabilized) by the inclusion of toroidal field components, first in 2.5D neglecting helical axis displacements, and consecutively in 3D, where also current-driven kinks may occur.

We acknowledge financial support from the FWO, grant G.027708, and from the K.U. Leuven GOA/09/009. Part of the computations made use of the High Performance Computing VIC cluster at K.U. Leuven. Z. Meliani acknowledge financial support from HPC Europa (project number: 228398). Visualization was performed using Paraview, see www.paraview.org.

REFERENCES

Appl, S., & Camenzind, M. 1993, A&A, 270, 71
Bacciotti, F., Mundt, R., Ray, T. P., Eisköffel, J., Solf, J., & Camenzind, M. 2000, ApJ, 537, L49
Bacciotti, F., Ray, T. P., Mundt, R., Eisköffel, J., & Solf, J. 2002, ApJ, 576, 222
Baty, H., & Keppens, R. 2002, ApJ, 580, 800
Begelman, M. C. 1998, ApJ, 493, 291
Begelman, M. C., & Li, Z. Y. 1994, 426, 269
Biretta, J. A., Junor, W., & Livio, M. 2002, New. Astron. Rev., 46, 239
Bogovalov, S., & Tsinganos, K. 2001, MNRAS, 325, 249
Coffey, D., Bacciotti, F., Ray, T. P., Eislöffel, J., & Woitas, J. 2007, ApJ, 663, 350
Coffey, D., Bacciotti, F., Woitas, J., Ray, T. P., & Eislöffel, J. 2004, ApJ, 604, 758
Cranmer, S. R. 2008, ApJ, 689, 316
Fendt, C. 1997, A&A, 319, 1025
Fendt, C. 2009, ApJ, 692, 346
Ghisellini, G., Tavecchio, F., & Chiaberge, M. 2005, A&A, 432, 401
Giroletti, M., et al. 2004, ApJ, 600, 127
Ghisellini, G., & Tavecchio, F. 2008, MNRAS, 386, L28
Gopal-Krishna, & Wiita, P. J. 2000, A&A, 363, 507
Günther, H. M., Matt, S. P., & Li, Z.-Y. 2009, A&A, 493, 579
Hardcastle, M. J. 2006, MNRAS, 366, 1465
Hardee, P. E. 2004, Ap&SS, 293, 117
Heyvaerts, J., & Norman, C. 2003, ApJ, 596, 1240
Istomin, Ya. N., & Pariev, V. I. 1996, MNRAS, 281, 1
Jester, S., Harris, D. E., Marshall, H. L., & Meisenheimer, K. 2006, ApJ, 648, 900
Jester, S., Meisenheimer, K., Martel, A. R., Perlman, E. S., & Sparks, W. B. 2007, MNRAS, 380, 828
Kataoka, J., et al. 2008, ApJ, 685, 839
Keppens, R., Meliani, Z., van der Holst, B., & Casse, F. 2008, A&A, 486, 663
Komissarov, S. S., Barkov, M. V., Vlahakis, N., & Königl, A. 2007, MNRAS, 380, 51
Matsakos, T., Tsinganos, K., Vlahakis, N., Massaglia, S., Mignone, A., & Trussoni, E. 2008, A&A, 477, 521
McKinney, J. C., & Blandford, R. D. 2009, MNRAS, 394, L126
Meier, D. L. 2003, New Astron. Rev., 47, 667
Mignone, A., & Bodo, G. 2005, MNRAS, 364, 126
Mignone, A., Plewa, T., & Bodo, G. 2005, ApJS, 160, 199
Mizuno, Y., Lyubarsky, Y., Nishikawa, K.-I., & Hardee, P. E. 2009, ApJ, 700, 684
Meliani, Z., Casse, F., & Sauty, C. 2006a, A&A, 460, 1
Meliani, Z., & Keppens, R. 2007, A&A, 475, 785
Meliani, Z., Keppens, R., Casse, F., & Giannios, D. 2007, MNRAS, 376, 1189
Meliani, Z., Keppens, R., & Giacomazzo, B. 2008, A&A, 491, 321
Meliani, Z., Sauty, C., Tsinganos, K., & Vlahakis, N. 2004, A&A, 425, 773
Meliani, Z., Sauty, C., Vlahakis, N., Tsinganos, K., & Trussoni, E. 2006b, A&A, 447, 797
Narayan, R., Li, J., & Tchekhovskoy, A. 2009, ApJ, 697, 1681
O'Sullivan, S. P., & Gabuzda, D. C. 2009, arXiv:0907.5211
Racusin, J. L., et al. 2008, Nature, 455, 183
Rawlings, S., & Saunders, R. 1991, Nature, 349, 138
Siemiginowska, A., Stawarz, L., Cheung, C. C., Harris, D. E., Sikora, M., Aldcroft, T. L., & Bechtold, J. 2007, ApJ, 657, 145
Sol, H., Pelletier, G., & Assero, E. 1989, MNRAS, 237, 411
Spruit, H. C. 2009, arXiv:0804.3096
Spruit, H. C., Foglizzo, T., & Stehle, R. 1997, MNRAS, 288, 333
Tavecchio, F., Maraschi, L., Sambruna, R. M., Urry, C. M., Cheung, C. C., Gambill, J. K., & Scarpa, R. 2004, ApJ, 614, 64
van der Holst, B., & Keppens, R. 2007, J. Comput. Phys., 226, 925
van der Holst, B., Keppens, R., & Meliani, Z. 2008, Comput. Phys. Commun., 179, 617
Woitas, J., Bacciotti, F., Ray, T. P., Marconi, A., Coffey, D., & Eislöffel, J. 2005, A&A, 432, 149